Leveraging Single-Cell Transcriptomics of Developing Rat Ocular Outflow Tissues for Prioritization of Congenital Glaucoma Candidate Genes

Sean M. Martin[a,1], Kristina N. Whisenhunt[a,1], Stuart W. Tompson[a,b,*]

a Department of Ophthalmology and Visual Sciences, School of Medicine and Public Health, University of Wisconsin, Madison, Wisconsin, USA.

b McPherson Eye Research Institute, University of Wisconsin, Madison, Wisconsin, USA.

1 S.M. and K.W. contributed equally to this work.

* Corresponding author: Stuart W. Tompson, Dept. of Ophthalmology and Visual Sciences, University of Wisconsin-Madison, WIMR2, Rm 3457 1111 Highland Ave, Madison, WI 53705, USA.

Email: stompson@wisc.edu, swjt77@hotmail.com

ORCID identifier (ST): https://orcid.org/0000-0001-9788-6730

Author Contributions: S.T. designed the research; S.M., K.W., and S.T. performed the research; S.M., K.W., and S.T. analyzed the data; S.T. wrote the R code; and S.T. wrote the paper.

Competing Interest Statement: The authors declare no competing interest.

Classification: Biological Sciences, Cell Biology

Keywords: ocular outflow, Schlemm's canal, trabecular meshwork, single-cell transcriptomics, congenital glaucoma

ABSTRACT

Abnormal development of the intricate trabecular meshwork (TM) or Schlemm's canal (SC) structures in the eye can result in reduced aqueous humor fluid drainage and elevated intraocular pressure. If left untreated, these processes can lead to retinal ganglion cell loss, damage to the optic nerve, and infant-onset vision loss, termed congenital glaucoma. To identify gene expression important for development of these specialized aqueous humor outflow pathway (AHOP) structures, single-cell RNA sequencing was performed on rat AHOP tissues during three major periods of growth. High-quality transcriptomic profiles of 29,626 genes from 86,653 limbal cells were obtained and clustered into 13 general cell types. Refined identification of cell subtypes revealed 10,037 TM- and 546 SC-related cells that together showed enhanced expression of 395 genes compared to other limbal tissues. Interrogation of 44 genes known to be associated with Mendelian forms of childhood glaucoma revealed 36/44 (82%) were more highly expressed by SC/TM cells, whilst only 29/372 (8%) genes associated with complex later-onset glaucoma were specifically enriched. We propose prioritization of these selectively expressed genes during genome analyses of congenital/childhood glaucoma patients as they represent strong novel candidates for disease-causing variants. The transcriptomic dataset derived from these critical developing eye structures will also aid the generation of polygenic risk score estimates tailored toward early-onset glaucoma with underlying complex genetics.

SIGNIFICANCE STATEMENT

This study presents the first single-cell RNA sequencing dataset of the developing aqueous humor outflow pathway (AHOP), offering insight into the genes important for forming the tissues primarily affected in congenital/childhood-onset glaucoma. By profiling limbal cells from developing rat eyes, key AHOP cell populations, which constitute the trabecular meshwork (TM) and Schlemm's canal (SC), were identified via cell type-specific expression of known markers. This enabled examination of gene

expression associated with childhood- and adult-onset glaucoma in these developing cell types and revealed 395 selectively expressed genes. These findings provide a foundational resource to understand early AHOP development, identify novel candidate disease genes, and reveal molecular targets for glaucoma prevention and therapy.

INTRODUCTION

In the eye, aqueous humor (AH) is a clear fluid produced by the ciliary body that flows through the anterior chamber, delivering nutrients, clearing metabolic waste, and helping maintain ocular shape for focused vision. AH production is balanced via drainage through structures located at the interface between the cornea and iris – the conventional AH outflow pathway (AHOP). To prevent excess intraocular pressure (IOP), fluid exits the eye through the trabecular meshwork (TM) and Schlemm's canal (SC), which connects to the systemic blood circulatory system via collector channels (Fig. 1). Failure to correctly develop these intricate outflow structures can lead to elevated eye pressure, damage to retinal ganglion cells and the optic nerve, and early-onset vision loss known as congenital glaucoma.

The molecular mechanisms of congenital glaucoma have been elucidated in only 25% of cases, and all involved genes critical for the proper formation and function of the TM and/or SC tissues.(1-4) Our understanding of genes important for AHOP development has been restricted by the limited availability and complex heterogeneity of these early tissues. Several studies have recently employed single-cell RNA sequencing (scRNAseq) to catalogue gene expression in outflow tissues from humans, nonhuman primates, pigs and mice,(5-9) but all profiled mature tissues. To date, no study has attempted to identify the cells and molecular pathways active during the early development and growth of the TM and/or SC tissues relevant to the etiology of congenital glaucoma.

The mature TM is a sieve-like structure composed of three distinct layers, each contributing to the regulation of AH outflow and IOP.(10) AH first passes through the uveal meshwork – a loose, open network of connective tissue encased in a continuous basement membrane and lined with endothelial-like TM cells (TMCs). This layer serves to filter larger cellular debris and neutralizes reactive oxygen species (ROS). The middle corneoscleral layer consists of TMC-covered collagen and elastin-rich beams with smaller pores for finer filtration and additional ROS scavenging. Finally, the juxtacanalicular tissue (JCT), composed of loosely arranged extracellular matrix (ECM) and star-shaped fibroblast-like TMCs, regulates AH outflow resistance in coordination with the inner wall of SC.(11) The mature SC is composed of a monolayer of vascular endothelial cells that share molecular characteristics with blood and lymphatic endothelial cells.(12, 13) The SC endothelial cells (SECs) can be divided into inner-wall (IW) cells that lay against the TM and outer-wall (OW) cells located towards the outside of the eye. The IW allows AH outflow through giant vacuoles and pores whilst maintaining a blood-aqueous barrier, whereas the OW maintains the canal's structure and passes AH into collector channels that lead away from the eye.(14)

Here, we present a study utilizing scRNAseq to identify the major cell types and their associated gene expression profiles during three major stages of SC and TM development in rats. Rat tissues share all major stages of anterior chamber angle development and morphological characteristics of the AHOP with humans, and they also enable acquisition of larger quantities of relevant tissue components versus mice. Remé and colleagues performed detailed electron and light microscopy studies of rat AHOP development,(15) observing AHOP anlage formation at embryonic day 7. By postnatal day 5 (P5), the presumptive TM remained an undifferentiated condensation of periocular mesenchyme (POM), and a rudimentary cluster of blood vessels that would become SC were visible. Between P5 and P10, sheets of primitive TM formed, and the young SC vessels became enlarged. Between P10 and P20, the TM

became five or six layers with distinct cells and SC had fused into a vessel with a single vacuole. The final structures were formed between P20 and P60, when the TM became less dense with the formation of Fontana's spaces and beams, and both the TM and SC elongated into their mature forms. Based on these developmental observations, we profiled these specialized tissues at P7-9, P14-16, and P27-29.

RESULTS

Limbal Cell Acquisition

Histological examination of rat AHOP tissues at P8, P15, and P28 confirmed the morphological findings described by Remé and colleagues (Fig. 2A).(15) In total, three male and three female limbal tissue strips (region highlighted in Fig. 1) were dissected and dissociated into single-cell suspensions at each of the three developmental ages. Samples contained all cell types located between the cornea and sclera on the exterior surface of the eye to the ciliary body on the inner side. The final dataset contained transcriptomic profiles of 29,626 genes from 86,653 limbal cells, visualized as 13 major cell type clusters (C0-C12) according to overall gene expression similarity (Fig. 2B). The major cell type identities within these clusters were revealed through differential expression of published marker genes, as described in Supporting Information (Identification of Major Limbal Cell Types, Fig. S1).

Vascular Endothelium and the Identification of Schlemm's Canal Cells

Vascular endothelial cells (VECs), including those that form Schlemm's canal (SECs), uniquely express *Pecam1* and formed a single independent cluster (C8, Fig. S2). To specifically identify SECs, these 3,155 cells were reclustered into nine subtypes (VEC0-VEC8, Fig. 3A, Fig. S3). Their vascular identities were ascertained through interrogation of differentially expressed genes, as described in Supporting Information (Identification of VEC Subtypes, Fig. S3). In mice, SECs share transcriptional features of both blood and lymphatic endothelia, expressing *Cd34* and *Prox1*, but not *Pdpn* or *Vwf*, yet they also retain distinct gene expression patterns that reflect their specialized role in AH drainage.(9, 12, 13, 16) SECs expressing these hybrid features formed VEC1 and a subpopulation of VEC7 (Fig. 3A, Fig. S3). Consistent with the growth and maturation of SC, the SECs population (VEC1) dramatically increased with sample age (Fig. 3, Fig. S4). The two distinct SEC-related populations in VEC7 were formed from proliferating cells highly expressing *Top2a* and *Mki67*.(17, 18) These populations also changed in size with tissue age (Fig. S4). As SC developed, the larger population displaying a stronger blood vessel-like profile (high *Flt1*, *Lrg1*, *Stc1*, *Sema3e*, *Tcf15*, low *Prox1*) reduced in number, whilst the smaller island exhibiting more SEC-like expression became numerous. This was consistent with cells involved in the formation of SC - proliferating VECs shifting their expression profile during canalogenesis from blood vessel-like to a more hybrid-lymphatic phenotype and ultimately contributing to the more specialized SEC pool in VEC1.(12)

In mouse studies, SECs do not significantly express the *Lyve1* gene, which is restricted to lymphatic vessels and a subset of interstitial macrophages that preferentially localize near vessels.(9, 12, 13, 16, 19) In contrast, our studies in rat have revealed *Lyve1* expression not only in lymphatic vessels and interstitial macrophages but also at low levels in more mature SECs (Fig. 3B). We confirmed this finding at the protein level, immunostaining whole mounted tissues for Pecam1 to visualize SC, Aif1 to broadly highlight macrophages, and Lyve1 (Fig. 3C).(20) At P4, areas of SC consisted of rudimentary smaller vessels that did not express Lyve1, and could be observed undergoing macrophage-aided vessel fusion (arrow). At P7, regions of SC comprised clustered vessels that were not fully fused and Lyve1 levels remained insignificant. At P14, Lyve1 expression by SECs was distinct from resident macrophages and was stronger towards the inner wall. At P28, Lyve1 expression by SECs was strongest

and remained primarily towards the inner wall, reflecting the acquisition of lymphatic-like properties by the mature outflow vessel.

Identification of SEC Subtypes

In total, 655 VECs with SC-like profiles were identified, comprising 109 actively proliferating cells and 546 that were quiescent and more specialized. To resolve further SEC heterogeneity, VEC1 and VEC7 cells were isolated and re-clustered, yielding six subpopulations with distinct gene expression profiles (SEC0-SEC5, Fig. 4; heatmap of top differentially expressed genes between SEC clusters provided in Fig. S5). To support this dataset, *in situ* hybridization (ISH) studies were performed on AHOP tissues to confirm the localized expression of key SEC markers (Fig. S6). The method used fluorescent probes to detect individual mRNA transcripts in and around cell nuclei in intact but thin tissue sections. Due to the limited number of nuclei captured from sections across the lumen of SC, this technique was only able to effectively localize robustly expressed genes. Furthermore, as observed for *Pecam1*, *Tek*, *Flt1*, and *Cd34*, transcripts were more readily detected in IW versus OW cells, despite their well-established expression throughout SC (Fig. S6).

SECs derived from VEC1 formed four subclusters, while SECs from VEC7 remained in two spatially isolated populations (SEC3 and SEC5) distinguished by strong expression of genes related to cell replication. SEC3 cells were most abundant during early SC development (P7) and expressed genes associated with angiogenic sprouting and proliferation, including *Top2a*, *Mki67*, *Car8*, *Enpp2*, and *Nostrin*.(17, 18, 21-23) In contrast, SEC5 cells lacked sprouting markers but expressed genes for lymphatic processes (*Prox1*, *Lyve1*, and *Nfatc1*,(24)) and vessel remodeling (*Sema3a*(25), *Sema3d*(26)). ISH studies of *Top2a* expression were unable to localize SEC3/SEC5 cells to a specific SC region (Fig. S6), which reflected their limited population at any age.

SEC2 cells were observed during mid-stage development of SC and displayed transcriptional features similar to SEC5 but without proliferation markers. Specifically upregulated expression was related to progenitor/stem cell identity (*Mast4*,(27) *Kit*(28)), leukocyte chemotaxis (*Sele*,(29)), motility (*Sh3pxd2b*(30)), ECM modification (*Adamts17*(31)), and angiogenesis regulation (*Nox4*,(32) *Vash1*(33)). The expression of *Sele* has previously been attributed to OW cells in adult mice.(9) ISH studies of *Sele* expression in whole tissues reflected the scRNAseq data, with transcripts more readily detected later in SC development, but the signal was too limited to confirm localization to a specific region such as the OW (Fig. S6). Conversely, *Nox4* expression signal was strong throughout AHOP development in both the IW and OW at P7 and P14 but appeared more restricted to the IW at P31 (Fig. S6).

The largest late-stage populations of SEC0 and SEC1 cells showed closely related profiles, including expression of a gap junction protein associated with lymphatic-like endothelia, *Gjc2*.(34) ISH studies of *Gjc2* localized the most robust expression to IW cells at P14 (Fig. S6). Specifically, SEC0 cells showed the strongest expression of *Gjc2* and *Hspb1*, a protein involved in endothelial movement.(35) Conversely, SEC1 cells exhibited enhanced expression related to lymphatic identity (*Prox1*, *Lyve1*, *Nfatc1*), vessel remodeling (*Sema3a*, *Sema3d*), regulation of angiogenesis (*Skil*(36), *Pgf*(37)), ECM remodeling (*Thsd4*(38)), and a chemokine that attracts immune cells toward lymphatic-like vessels (*Ccl21*(39, 40)). High *Prox1* and *Ccl21* expression have previously been associated with IW cells in adult mice.(9) Consistent with this, ISH studies of *Ccl21* identified low expression localized to the IW (Fig. S6). Furthermore, SEC1 cells also expressed genes that could be related to IW function, such as flow–responsive lymphatic remodeling (*Dtx1*(41, 42)), lumen maintenance (*Sh3gl3*(43)), and sodium transport (*Scn5a*(44)). The smallest late-stage population of SEC4 cells were enriched for genes

involved in integrin signaling (*Postn*(45)), cytoskeletal dynamics (*Wipf3*(46)), vascular integrity (*Plxna4*(47)), and maintenance of vascular homeostasis (*Nos1*(48)). Like SEC2, SEC4 cells also expressed *Sele*, which suggested they were derived from the OW.

While enhanced expression of the ECM component nephronectin (*Npnt*(49)) has been reported for a subset of IW cells in adult mice,(9) this gene was more broadly expressed in all rat SECs with particular enrichment in SEC4 (putative OW cells). Interestingly, both SEC1 (IW) and SEC4 (OW) cells shared expression of two genes previously identified in human lymphatics, *Mmrn1* and *Pkhd1l1*.(50) Finally, most SEC clusters selectively expressed a subunit of the sodium/potassium ATPase pump that is critical for cell volume maintenance (*Fxyd2*).(51) Given that *Fxyd2* expression in the rat limbus was otherwise restricted to monocytes, this gene emerged as one of the most specific markers for all SEC types in our dataset.

Identification of Trabecular Meshwork Cells Within Fibroblast-Like Populations

As demonstrated by Remé et al., in rats the TM begins forming as a condensed mass of multipotent periocular mesenchyme (POM) between P7-P9, which differentiates into primitive TM sheets.(15) These early POM cells express high levels of the developmental transcription factor *Pitx2*,(52) which is subsequently downregulated as they transition into TM cells (TMCs) - elongating, flattening, and becoming separated by extracellular fibers that organize into lamellae and connective tissue.(53) By P14-P16 the layered TM structures are evident, and by P27-P29 the tissue resembles mature architecture with a meshwork of beams and large Fontana's spaces.(15)

In the mature tissue, TMCs across all three layers express shared genes, including *Col4a1* and *Col8a1* (Type IV and VIII collagen alpha chains),(11) *Eln* (elastin),(54) *Nid1* (nidogen-1),(11) *Myoc* (myocilin),(7) *Mgp* and *Spp1* (calcification inhibitors),(55, 56) *Angpt1* and *Svep1* (angiogenic mediators),(8, 57) and *Ltbp2* (an ECM protein involved in TGF-β regulation).(58) TMCs also express *Acta2* (smooth muscle actin),(59) but not *Des* (desmin),(11) distinguishing them from smooth muscle cells. Unlike the adjacent corneal endothelia, TMCs do not express *Col4a3*, encoding the α3 chain of type IV collagen.(11)

Layer-specific functions of TMCs are reflected by their differential gene expression. TMCs of the uveal and corneoscleral layers secrete tissue plasminogen activator (*Plat*) to maintain pathway patency,(60) superoxide dismutases (*Sod1*, *Sod2*, *Sod3*) to combat reactive oxygen species (ROS),(61) and *Il6* for IOP regulation.(62) In primates, hyaluronic acid (HA) is present in the JCT ECM but it is not synthesized locally.(63) Instead, HA is produced by *Has1*/*2*/*3* in uveal and corneoscleral TMCs(63, 64) and is carried into the JCT by AH flow.(59) JCT-resident TMCs are identifiable by elevated expression of chondroadherin (*Chad*),(5) tenascin-C (*Tnc*),(65) angiopoietin-like 7 (*Angptl7*),(5-7) chitinase-3-like protein 1 (*Chi3l1*),(5) thrombospondin-1 (*Thbs1*),(66) and crystallin alpha B (*Cryab*).(11, 67)

To identify TMCs in the rat limbal dataset, cells were screened for high expression of the POM marker *Pitx2*, along with four genes previously localized to the TM: *Myoc*, *Angpt1*, *Svep1*, and *Ltbp2*.(7, 8, 58) These genes showed variable expression across several limbal clusters but all were strongly enriched in C1 (Fig. 5). Consequently, subsequent analyses were focused on this population of 21,735 fibroblast-like cells.

C1 cells were isolated and reclustered into four fibroblast-like (FBL0-FBL3) subtypes (Fig. S7A), and their identities inferred from established marker genes, as described in Supporting Information (Identification of FBL Subtypes, Fig. S7B; heatmap of top differentially expressed genes between FBL clusters provided in S8). Putative TMC-like cells were identified within FBL0, isolated, and the 10,037

cells re-clustered into seven groups (TMC0-TMC6, Fig. 6; heatmap of top differentially expressed genes between TMC clusters provided in Fig. S9). The TMC cluster data correlated with ISH studies in tissue sections, which showed expression of the pan-TM marker *Myoc* increased progressively with tissue maturation, starting posterior to the rudimentary SC and spreading throughout the TM as it developed (Fig. S10). Conversely the *Cyp1b1* gene, in which mutations account for most congenital glaucoma with a molecular diagnosis, was expressed more highly in P7 and P14 TMCs than at P31 (Fig. S11).

To investigate the developmental trajectory of these subpopulations, we analyzed changes in cell abundance across developmental timepoints. Cell populations in TMC1, TMC2, and TMC4 decreased over time, suggesting they represent progenitor or transitional states (Fig. 6A). Notably, TMC2 cells exhibited a marked shift in UMAP position, indicating broad changes in expression profile as the TM developed. TMC5 cells largely maintained their numbers, while TMC6 cells gradually expanded - both accompanied by dynamic changes in gene expression. In contrast, TMC0 and TMC3 expanded significantly during mid-to-late developmental stages, which implicated them as terminally differentiated TMCs. Minimal expression of proliferation (*Mki67*, *Top2a*) and apoptosis (*Casp3*, *Casp7*(68)) markers suggested cell state differentiation as the major cause of the cluster changes.

The largest terminal cluster, TMC0, showed the strongest *Myoc* expression but contained few cells at P7 (Fig. 6A). This population expanded substantially over time and expressed hallmark markers of the JCT, including *Chad*, *Angptl7*, *Chi3l1*, and *Thbs1*.(66) Additional genes enriched in TMC0 cells included *Pla2g2a*, *Shisa3*, *Ccn5*, *Cilp2*, *Podnl1*, and *Nrgn*. ISH studies of *Chad* detected strong expression in corneal and limbal stroma and confirmed weaker expression within a subset of the TM that localized more closely to the JCT at P31 (Fig. S12).

The second and third largest terminal clusters, TMC3 and TMC6, expressed key markers of the uveal and corneoscleral TM layers, including *Plat* (tissue-type plasminogen activator), *Il6* (interleukin-6), and *Sod2* (superoxide dismutase 2).(60-62) The clusters also expressed *Vcan* (versican), which binds HA to form large proteoglycan aggregates and plays a role in modulating AH outflow resistance in the JCT(69, 70), and the metalloprotease *Adamts1*, which cleaves versican into its bioactive form.(71) These data suggest that, like HA, versican is secreted by uveal and corneoscleral TMCs and transported into the JCT by aqueous flow.(63) TMC3 and TMC6 cells also expressed *Gsn*, *Ctsc*, *Heyl*, and the TM lamellae-associated type V collagen (*Col5a3*(72)). ISH studies of *Gsn* detected moderate expression widely throughout the P7 and P14 tissues which became strongly enriched in the TM layers by P31 (Fig. S13). Specifically, TMC3 cells could be distinguished by selective expression of *Apoe*, *Nav3*, *Crlf1*, *Csmd1*, and *Pdlim3*. ISH studies of *Apoe* confirmed selective expression within a subset of the TM (Fig. S14). Conversely, TMC6 cells uniquely expressed HA synthase (*Has1*),(63, 64) TM-associated mechanosensitive ion channel (*Piezo2*),(73) *Clec3b*, *Sema3d*, *Pi16*, *Ccl11*, *Edn3*, *Gsta1*, *Enpp3*, *Enpp1*, and *Ccl7*. ISH studies for *Clec3b* confirmed expression localized to a specific subset of the TM at P14 and P31 (Fig. S15).

Significant TMC2 and TMC5 cell populations were present at all three developmental ages with subtle changes in cluster locations noted, reflecting overall gene expression shifts. TMC2 cells shared a similar profile to TMC0, that included JCT-like *Chad* and *Angptl7* expression, but with higher levels of *Fos* and *Egr1*. ISH studies of *Fos* localized specific expression to the posterior region of the TM at P7 and P14 that was adjacent to SC by P31 (Fig. S16). In contrast, TMC5 cells displayed a transcriptional profile that included the strongest markers for tendon (*Tnmd*(74)) and smooth muscle (*Acta2*, *Tagln*, *Myl9*, *Eln*), as well as unique expression of *Grid2* and *Cit*. ISH studies of *Tnmd* detected highly specific expression throughout the TM at P7 and P14 that extended to adjacent stromal fibroblasts by P31 (Fig. S17).

Finally, the two early-stage TM populations (TMC1 and TMC4) were significantly reduced by P28, which was consistent with progenitor cells contributing to TM formation. Both clusters expressed high levels of *Chad* and *Angptl7*, supporting their identity as JCT progenitors. Other genes expressed by TMC0/JCT cells were also detected at higher levels in TMC1 cells, such as *Igfbp2*, *Pdgfrl*, *Col8a1*, and *Nrgn*. ISH studies of *Igfbp2* confirmed strong expression throughout the early TM at P7 that persisted at P31 (Fig. S18). Early stage TMC1 cells also shared expression of *Dlk1* with the later TMC2 and TMC5 cell types. Conversely, TMC4 cells were marked by higher levels of *Tgfbi*, a protein important for cell-ECM interactions,(75) which ISH studies confirmed peak expression at P14 in TMCs located between SC and the ciliary body (Fig. S19).

Selective Gene Expression in SECs and TMCs

In total, this study identified 655 SC- and 10,037 TM-related cells that could be further subdivided into 13 distinct populations according to their distinguishing gene expression profiles. To recognize molecular pathways important for the development and function of SC and the TM, differential expression analyses were performed to identify genes with enhanced expression in these important cell types versus all other limbal cells. For the four main SEC subtypes (SEC0, SEC1, SEC2, and SEC4), 244 genes with human orthologs were selectively expressed in one or more of the subclusters. Genes selectively expressed by the proliferating BEC population (SEC3) were not included as these cells could not be definitively related to SC versus other developing blood vessels. Only *Hoxd8*, a transcription factor important for the differentiation of BECs into lymphatic-like endothelial cells,(76) was selectively expressed in the proliferating SEC population (SEC5) compared to SEC3 cells. Its inclusion brought the total number of selectively upregulated SEC genes to 245. In total for all seven TMC subtypes, 153 genes with human orthologs were selectively upregulated in one or more of the subclusters. Three genes, *Ephb1*, *Lbp*, and *Sema3d*, were identified in subtypes of SECs and TMCs. Combined, this study identified 395 genes selectively upregulated in cell types associated with these two critical developing outflow pathway tissues (Fig. 7).

Gene Expression Associated with Mendelian Disease

We sought to assess whether genes already associated with Mendelian forms of congenital glaucoma are expressed within our developing SC/TM dataset. Congenital glaucoma falls within a larger group of developmental anomalies collectively referred to as anterior segment dysgenesis (ASD; OMIM 107250). These conditions show a vast phenotypic variability of abnormalities affecting the iris, cornea, lens, TM, and SC,(77) and are caused by mutations in many genes including *PAX6*, *FOXC1*, *PITX2*, *FOXE3*, *PITX3*, *PXDN*, *CPAMD8*, *B3GLCT*, and *COL4A1*.(77-79) It can be difficult to diagnostically separate cases of primary congenital glaucoma from the other ASD disorders when the clinical features outside of the drainage tissues are mild.(78, 79) Furthermore, there are numerous syndromic forms of congenital glaucoma encompassing non-ocular organ systems. These disorders are also highly variable in their clinical manifestations and individuals may or may not present with childhood glaucoma. Together, this study interrogated 44/45 genes previously associated with congenital glaucoma. One gene, *Guca1c*, could not be assessed in our data due to the lack of a rat ortholog. The data revealed 36/44 (82%) genes were expressed by at least one SC- or TM-related cell cluster (Fig. 8).

Gene Expression Associated with Complex Disease

Genome-wide association studies (GWAS) have implicated hundreds of genes in the pathogenesis of glaucoma. Primary open-angle glaucoma (POAG), the leading cause of irreversible blindness worldwide, is characterized by late-onset optic nerve damage, progressive visual field loss, and typically elevated IOP despite open access of AH to the drainage tissues.(80, 81) In 2021, Gharahkhani et al.

reported a multi-ethnic meta-analysis of GWAS data from 34,179 POAG cases and 349,321 controls, and identified 127 risk loci that collectively explained 9.4% of familial risk.(82) Of these, 89/123 loci with available IOP data were significantly associated with IOP, which suggested shared genetic etiology. More recently, Han et al. (2023) reported the largest multitrait gene-based GWAS analysis (MTAG), which identified 355 genes significantly associated with POAG risk.(83)

Given the expected role of AHOP dysfunction in POAG, we examined the expression of these POAG-associated genes in our dataset. Genes were filtered to remove duplicates between the two GWAS lists, those without known protein-coding rat orthologs, or those lacking expression in our scRNAseq data. In cases where multiple protein-coding genes mapped to a single locus, all were included in the assessment. Together, 372 POAG-associated genes were interrogated across SC/TM-related cell clusters (Fig. S20). Many of the genes demonstrated high expression in SECs and/or TMCs, but few were selectively expressed in just those cells versus other limbal cell types. Thirteen genes were selectively expressed at significant levels by SECs, which were *Adam15*, *Cav1*, *Cav2*, *Clic5*, *Cttnbp2*, *Egln3*, *Emid1*, *Fam53b*, *Kctd20*, *Maff*, *Pthlh*, *Tes*, and *Thsd7a*. Fourteen genes were selectively expressed at significant levels by TMCs, which were *Angpt1*, *Col24a1*, *Efemp2*, *Itgb5*, *Ltbp1*, *Ltbp2*, *Ltbp3*, *Myoc*, *Nucb2*, *Pitx2*, *Rora*, *Svep1*, *Tcf7l2*, and *Tgfb3*. Two genes, *Pde7b* and *Plce1*, were selectively enriched at significant expression levels in populations of both SECs and TMCs.

DISCUSSION

This work has demonstrated the feasibility of the scRNAseq approach to broadly catalogue cell types and their associated gene expression profiles in the diminutive and complex tissues of the developing rat AHOP. This method has identified 655 VECs related to SC development, including 109 actively proliferating and 546 quiescent, as well as 10,037 cells related to the development of the TM. ISH studies reinforced the localization of these cell types to SC/TM. Further refinement to specific regions, implicated by known marker gene expression, was restricted by limited rat tissue size and low nuclear transcript signals obtained from thin sections. As antibodies proven for rat protein detection become available, further whole tissue staining studies will enable a more detailed investigation.

Importantly, 395 genes were detected as selectively upregulated during the development of SC/TM. Furthermore, numerous marker genes have been identified that can distinguish cell subtypes which will aid future studies. Additional noteworthy genes significantly upregulated by SC-related cells were *Agt*, *Ccl2*, *Cdkl1*, *Chst3*, *Clic2*, *Dapk2*, *Lbp*, *Mmrn1*, *Myzap*, *Tbx1*, and *Trim16*. For TM-related cell types, prominent genes included *Adamtsl3*, *Epha3*, *Fmod*, *Itga11*, *Nkd2*, *Phactr4*, and *Prelp*. These genes are likely critical for the development and/or function of the AHOP and warrant further investigation. We propose prioritization of these genes during patient genome analyses as they represent strong novel candidates for congenital glaucoma-causing variants.

Unexpectedly, our studies revealed expression of *Lyve1* in rat SECs. This is in contrast to expression reported for SC in mice, where *Lyve1* expression is only associated with resident macrophages and not SECs.(12) *Lyve1* expression is controlled by specific signaling pathways, such as those involving *Prox1*, and encodes a hyaluronan receptor that primarily helps regulate the transport of immune cells and fluid through lymphatic vessels.(84) This function is distinct from that of blood vessels, which largely manage nutrient movement and gas exchange; consequently *Lyve1* is not expressed by BECs. However, SC is known to show hybrid characteristics of lymphatic and blood vasculature, expressing BEC-like *Cd34*, *Flt1*, *Nos3*, and LEC-like *Prox1*. Like lymphatic vessels, SC is highly involved in fluid homeostasis and immune cell trafficking from the eye, for which *Lyve1* may play a role. Our data is

consistent with this function for *Lyve1* in the SC of rats with expression that is negligible in early SECs but upregulated as the cells mature and acquire a lymphatic-like state.

Interrogation of 44 genes already associated with Mendelian forms of congenital glaucoma revealed 36/44 (82%) were expressed by at least one SC- or TM-related cell cluster. The classification of cell types presented here is consistent with published studies such as the expression of *Angpt1*, *Angptl7*, *Cyp1b1*, *Ltbp2*, *Myoc*, *Piezo1*, *Pitx2*, *Svep1*, and *Thbs1* in the TM,(3, 5-8, 57, 58, 66, 85, 86) and *Col4a1*, *Piezo2*, *Tek*, and *Tie1* in SC.(2, 12, 73, 87) Furthermore, for the eight genes which lacked SC/TM cluster expression, published findings describe expression and disease mechanisms that involve tissues outside of the conventional outflow pathway or functions required earlier in development. Specifically, *CPAMD8* variants cause congenital glaucoma with anterior segment dysgenesis, myopia, and ectopia lentis, likely due to abnormal iris or lens morphology rather than SC/TM defects.(79, 88) *CRYBB2*, associated with congenital cataracts and glaucoma, is expressed in lens epithelial cells and retinal neurons, and directly prevents RGC loss.(89-91) *FOXE3* and *PITX3*, both involved in early lens development, are linked to anterior segment dysgenesis, with lens-cornea or iris-lens adhesions obstructing aqueous outflow.(92-94) *PRSS56* mutations cause posterior microphthalmia, leading to angle-closure glaucoma due to a shallow anterior chamber.(95) *MAB21L1* mutations, associated with syndromic and ocular abnormalities including buphthalmos, impair anterior segment architecture in zebrafish, reducing outflow via fibrous masses between the lens and cornea.(96-99) *PAX6* is essential for early differentiation of periocular mesenchyme, and its loss in mice leads to an undeveloped TM and absent SC – events occurring too early in development (P0-P4) to be captured in this study.(100-102) Similarly, *GPATCH3* is implicated in congenital glaucoma, but its expression has only been observed in early zebrafish periocular mesenchyme and corneal endothelium.(103)

The identification of novel single gene causes of congenital glaucoma have not been forthcoming despite large-scale sequencing efforts. It is likely that there are many undiscovered genes in which strong-effect variants account for a limited proportion of the disease, but these are difficult to identify in individuals or small-sized patient cohorts. Utilizing the transcriptomic resource presented here, interrogation of variants in developing AHOP-expressed genes can now be prioritized. It is also probable that a proportion of the disease may not follow simple Mendelian inheritance patterns and instead involve complex polygenic mechanisms. Hundreds of genes have already been associated with glaucoma endophenotypes by GWAS, and investigators are now utilizing this knowledge to generate polygenic risk scores (PRS) – an approach that estimates an individual's disease risk based on their overall genetic makeup. This transcriptomic dataset will help adjust the weighting of variants in genes more highly expressed during AHOP tissue development, which in turn will enable the generation of PRS estimates tailored towards early-onset forms of glaucoma.

MATERIALS AND METHODS

Ocular Tissue Acquisition

Fischer 344 (F344/NCrl, Charles River Laboratories) rats, an albino, inbred strain of the common rat (*Rattus norvegicus*), were bred using standard husbandry practices. Staggered breeding pairs were established to collect all 18 limbal tissue strips within a three-day window. To minimize acquisition bias, dissections were performed in six groups, systematically changing the ascertainment order across genders and developmental age (Table S1). Eyes were enucleated and immediately placed in ice-cold Hanks' Balanced Salt Solution (HBSS) without calcium. Extraocular muscle was removed, and a scalpel was used to make an incision in the sclera just posterior to the limbus. Fine spring scissors were used to cut circumferentially around the globe to isolate the anterior cup. The lens and retina were removed, and

the anterior cup was bisected through the pupil with a scalpel. The iris was trimmed to retain only a small region adjacent to the ciliary body. The opaque sclera was dissected away just posterior to the ciliary body, and the clear cornea was excised immediately anterior to the limbus. The resulting limbal tissue strips were maintained in ice-cold calcium-free HBSS until all three samples in the group were ready for simultaneous dissociation.

Limbal tissue strips were enzymatically dissociated into single cells using a two-step protocol. First, the tissue was digested with Collagenase Type 1 (CLSS-1, 10 mg/mL; Worthington) in HBSS supplemented with calcium and magnesium at 37°C for 1.5 hours, with gentle inversion every 15 minutes. Following centrifugation at 300 RCF for 5 minutes (a condition used for all subsequent centrifugation steps), the pellet was further digested with TrypLE at 37°C for 20 minutes. During this step, samples were inverted at 5 and 10 minutes and gently pipetted with a wide-bore P1000 tip at 15 and 20 minutes to enhance dissociation.

After centrifugation, the largely dissociated cells were resuspended in ice-cold DMEM supplemented with 10% FBS. Residual tissue was gently dissociated by pipetting with a regular-bore P1000 tip. The cell suspension was filtered through a 70 µm Flowmi tip, centrifuged, and resuspended in 100 µL by pipetting with a wide-bore P200 tip, followed by a regular-bore P200 tip. The sample was then passed through a 40 µm Flowmi tip. Cell count and viability were assessed with a LUNA FX7, ensuring 11,200 viable single cells (>75% viability) were prepared for each sample. Cells were loaded into a well of a Chromium Next GEM Chip G, and Single-Cell 3′ Gene Expression libraries generated following the manufacturer's protocol (Chromium Next GEM Single-Cell 3′ Reagent Kit v3.1 User Guide, Rev D).

Single-Cell RNA Sequencing and Bioinformatic Processing

Eighteen dissociated tissue samples were independently processed through 18 GEM wells for 3' cDNA library construction. A preliminary low-read-deep sequencing run was conducted on an Illumina MiSeq to estimate the total cell counts and reads per cell across libraries. Quality control was performed using UMI-tools.(104) The 18 libraries were balanced, pooled, and deeply sequenced on a single S4 flow cell using the Illumina NovaSeq platform. Demultiplexing was performed with Cell Ranger's mkfastq command, utilizing Illumina's bcl2fastq wrapper. Subsequent alignment, filtering, and UMI counting for each sample was completed using the count command, in accordance with 10x Genomics' documentation. Reads were aligned to the latest rat genome reference (GRCr8, GenBank GCA_036323735.1, Jan 31, 2024) with the mitochondrial reference contig added from an earlier genome build (Rnor_6.0). Alignments included introns to enhance expression sensitivity and excluded pseudogenes to improve mapping quality.

Cell Ranger generated barcode matrices for each sample, which were aggregated using the aggr command. Unique GEM well suffixes were appended to barcodes to retain sample identity. Aggregation included depth normalization, ensuring equal average read depth per cell across samples to avoid sequencing depth-related artifacts. As all libraries were sequenced together in a single flow cell, no batch correction was necessary. The final aggregated matrix comprised raw normalized expression data from 126,787 gel bead droplets that were suitable for comparative analyses.

Bioinformatic Analyses

Data analysis was conducted primarily with the Seurat v 5.0.1 R package.(105) A Seurat object was created from the aggregated barcode matrix, including genes expressed in at least five cells. Low-quality cells were filtered out based on the following criteria: UMI count < 3000, fewer than 1200 genes expressed, or mitochondrial gene content > 10%. Mitochondrial content was calculated across 13

protein-coding mitochondrial genes (Mt-co1, Mt-nd6, Mt-atp6, Mt-co2, Mt-co3, Mt-nd3, Mt-nd1, Mt-nd4, Mt-nd5, Mt-atp8, Mt-nd2, Mt-nd4l, Mt-cyb). This filtering reduced the initial 126,787 cells to 90,274 high-quality cells.

Multiplets were detected and removed (~4%) using scDblFinder, yielding a final dataset of 86,653 single cells and 29,626 genes. Expression data were normalized using Seurat's NormalizeData function, which scales gene counts per cell to 10,000, followed by log transformation.

For dimensional reduction and clustering, Seurat's SCTransform function was used to normalize, scale, and identify variable genes. Principal component analysis was performed using RunPCA, and an elbow plot determined that the first 18 principal components captured most variance. A Shared Nearest Neighbor (SNN) graph was constructed with FindNeighbors, and clustering was done using FindClusters (resolution = 0.1). A two-dimensional Uniform Manifold Approximation and Projection (UMAP) was generated with RunUMAP, visualizing 13 distinct cell-type clusters according to each cell's overall gene expression similarity.

Differential gene expression was assessed using the FindMarkers command in conjunction with the Model-based Analysis of Single-cell Transcriptomics (MAST) algorithm - a statistical tool that models gene expression via a zero-inflated hurdle model to account for sparsity specifically in single-cell datasets.(106) For TMCs, the criteria for selective expression were a greater than two log2 fold change upregulation in more than 20% of cells within the TMC subcluster versus all other limbal cells and robust expression (significant UMI counts or highly cluster-specific UMIs at low level). For SECs, as all the VECs are very different to other limbal cells, a more stringent criteria needed to be implemented with expression thresholds set at a greater than two log2 fold change upregulation in more than 30% of cells within the SEC subcluster versus all other limbal cells, less than 10% expression in other limbal cells, and robust expression (significant UMI counts or highly cluster-specific UMIs at low level).

UMAP and HeatMap plots were generated using the standard Seurat package commands DimPlot and DoHeatMap, respectively. Customized DotPlot and FeaturePlot (individual gene expression overlayed on UMAP) images were generated using the DotPlot_scCustom and FeaturePlot_scCustom commands within the scCustomize package (https://doi.org/10.5281/zenodo.5706430).(107)

Whole Mount Fluorescent Immunohistochemistry (Lyve1, Aif1, and Pecam1)

Fischer rats were euthanized via decapitation at P4 and P7 or CO2 gas inhalation at P14 and P28. Eyes were rapidly enucleated and placed in ice-cold 1x phosphate buffered saline pH 7.4 (PBS). Eyes were punctured with a 30G needle posterior to limbus, and immersion fixed in 4% paraformaldehyde (PFA) in PBS for 10 minutes at 4°C. Following fixation, tissues were washed in 70% ice-cold molecular biology grade ethanol (EtOH) and stored in fresh 70% EtOH at 4°C. For staining, eyes were transferred to a Kimwipe soaked in ice-cold PBS for dissection. Using spring scissors and fine tip forceps, extraneous tissues such as the conjunctiva, muscle, and tendon were removed, eyes bisected, and lenses extracted. Anterior eye cups were transferred into a dish containing ice-cold PBS where the retina and ciliary body were removed. The tissues were placed into blocking/staining buffer (5% normal donkey serum (Cat. 017-000-121, Jackson ImmunoResearch Labs) 0.5% triton x-100, and 0.01% sodium azide in PBS) on a nutator overnight at 4°C. Blocking buffer was replaced with primary antibodies diluted in staining buffer and incubated on a nutator at 4°C for approximately 24 hours. Mouse anti-CD31/PECAM1 (Cat. MA1-80069, Invitrogen) was diluted 1:100, rabbit anti-LYVE-1 (Cat. 67538, Cell Signaling) at 1:500, and goat anti-AIF-1 (Cat. NB100-1028, Novus) at 1:100. Primary antibodies were removed, and eye cups washed three times in PBS containing 0.01% Tween 20 for one hour at room temperature (RT). Secondary antibodies diluted in staining buffer were added and tissues incubated on a nutator at 4°C for

approximately 24 hours. Donkey anti-mouse Alexa 405 (Cat. A48257, Invitrogen) was diluted at 1:500, donkey anti-rabbit Alexa 546 (Cat. A10040, Invitrogen) at 1:500, and donkey anti-goat Alexa 647 (Cat. 705-605-147, Jackson ImmunoResearch Labs) at 1:500. Following secondary antibody removal, tissues were washed four times with PBS containing 0.01% Tween 20 for 1 hour at RT. Eye cups were transferred into cold PBS and a series of relief cuts were made towards the center that resulted in a flower petal appearance. Tissues were placed on glass microscope slides with the cornea side down, excess fluid removed, and mounted (Shandon-Mount, Cat. 1900331, Epredia) with #1.5 coverslips. Slides were dried for >16 hours at 4°C and imaged with a Nikon A1R confocal microscope using a 20x objective and 23 um pinhole (1 Aery unit). A 75 um Z-stack of 1 um slices was collected, which encompassed all of SC.

In Situ Hybridization (RNAscope)

Rats were euthanized by decapitation (P7) or CO2 gas inhalation (P14 and P31). The eyes were rapidly enucleated and transferred into ice-cold 4% PFA in 1x PBS, pH 7.4 (4% PFA). Using a scalpel, a large incision was made posteriorly to the limbus to allow rapid PFA access to internal eye structures. Tissues were placed into fresh ice-cold 4% PFA at 4°C for 2 hours. Eyes were dissected in 4% PFA on ice, removing extraneous muscle and tendon, bisecting posterior to the limbus, and removing the lens. Fixation of the anterior eye cups continued in 4% PFA at 4°C for a total of 20 hours. Tissues were processed through an alcohol series, xylene, and embedded in paraffin. Blocks were stored at 4°C in a sealed container with desiccant. Paraffin blocks were sectioned at 5 µm thickness and allowed to dry overnight at RT. Sections were processed for RNAscope following the manufacturers protocol (User Manual for RNAscope Multiplex Fluorescent Reagent Kit v2, UM 323100/rev B/Effective Date: 10/11/2022). Mild conditions were used for antigen retrieval (10 minutes) and standard conditions for the protease treatment (30 minutes). Hybridization was performed in a HybEZ II oven (Cat. 321710/321720). Details of RNAscope probes are provided in Table S3, which were used in conjunction with the following Opal dye fluorophores (Akoya Biosciences): Opal 520 (Cat. FP1487001KT), Opal 570 (Cat. FP1488001KT), Opal 620 (Cat. FP1495001KT), and Opal 650 (Cat. FP1496001KT). Images were collected with a Nuance Multispectral Imaging System including an Olympus BX43 microscope with 40x objective and Perkin Elmer Nuance software v.3.0.2).

DATA AVAILABILITY

The raw data files from this study have been deposited in the Sequence Read Archive of the National Center for Biotechnology Information (accession no. TBD).

ACKNOWLEDGMENTS

This study was funded by NIH/NEI R21 EY034251 (S.W. Tompson). This work was also supported by the Margaret Emma Williams Trust Fund to the UW-Madison Department of Ophthalmology and Visual Sciences, an Unrestricted Grant from Research to Prevent Blindness, Inc. to the UW-Madison Department of Ophthalmology and Visual Sciences, and a Core Grant for Vision Research from the NIH to the University of Wisconsin-Madison (P30 EY016665).

The authors utilized the University of Wisconsin-Madison Biotechnology Center's Gene Expression Center (Research Resource Identifier – RRID:SCR_017757) for 10X Genomics scRNAseq library preparation, DNA Sequencing Facility (RRID:SCR_017759) for Illumina sequencing, and Bioinformatics Core Facility (Research Resource Identifier – RRID:SCR_017799) for initial processing of raw scRNAseq data. The authors also wish to thank the University of Wisconsin Translational Research Initiatives in Pathology (TRIP) Laboratory, supported by the UW Department of Pathology

and Laboratory Medicine, UWCCC (P30 CA014520) and the Office of The Director- NIH (S10 OD023526) for its histology and RNAscope services, and for the use of their facilities. Confocal imaging was facilitated by the University of Wisconsin Optical Imaging Core, and we thank Lance A Rodenkirch for microscopy support.

We thank the DOVS department chair, Dr. Terri L. Young, for provision of technical support staff, laboratory space, and start-up funding. The authors would also like to thank Dr. Abigail Radcliff in the laboratory of Dr. Jyoti Watters (UW School of Veterinary Medicine), and Miranda Pamperin, Riley Brutto, Devin Larson, and John Michael in the laboratory of Dr. Edwin Chapman (UW Neuroscience) for providing rat tissues for preliminary studies. We also thank Dr. Stephanie L. Nay for critical review of the manuscript.

FIGURES AND TABLES

Fig. 1: Route of aqueous humor outflow at the junction of the cornea and iris. H&E-stained tissue section from a mature (postnatal day 80) rat anterior eye segment. Blue arrows illustrate the outflow route of aqueous humor through the trabecular meshwork (TM) and Schlemm's canal (SC). Tissues dissected for scRNAseq profiling are highlighted (blue dashed box).

Fig. 2: Morphology of dissected developing AHOP tissues and resulting scRNAseq clustering of complete limbal dataset. (A) H&E-stained anterior eye sections highlighting the AHOP tissues at P8, P15, and P28. Labels show primitive TM (PTM), primitive SC (PSC), trabecular meshwork (TM), Schlemm's canal (SC), and Fontana's spaces (FS). Scale bars 50µm. (B) Clustering of single-cell profiles visualized by two-dimensional Uniform Manifold Approximation and Projection (UMAP). The 13 major clusters are distinguished by different colors and numbered (C0-C12) by descending cell population. Cell type identities assigned by key marker gene expression (Fig. S1) are smooth muscle cells (SMC), fibroblasts (FIBR), pigmented epithelium (PIEP), pericytes (PERI), melanocytes (MELA), monocytes-1 (MON1), nonpigmented ciliary epithelium (NPCE), surface epithelium (EPI), vescular endothelial cells (VEC), Schwann cells (SCHW), lymphocytes (LYMP), proliferating mesenchyme (PMES), and monocytes-2 (MON2).

Fig. 3: As SC develops in rats, a population of SECs express *Lyve1* as they take on a more lymphatic phenotype. (A) Reclustering of 3,155 VECs from the limbal C8 population visualized by UMAP in nine subtypes (VEC0-VEC8). (B) *Lyve1* expression throughout the VEC dataset (normalized log2 fold change expression). (C) Whole mount anterior cup tissues stained with Pecam1 (blue) to visualize SC, Aif1+ (cyan) macrophages, and Lyve1+ (red) subsets of macrophages and SECs. Macrophage-aided fusion of rudimentary vessels shown at P4 (arrow). Images oriented SC inner wall down. Scale bars 50µm.

Fig. 4: Cellular subtypes and associated gene expression within the Schlemm's canal endothelial cell population during development. (A) UMAP plot of the six SEC subpopulations at the three developmental timepoints. (B) Dot plot of key marker gene expression distinguishing SEC subtypes.

Fig. 5: Limbal expression of *Myoc*, *Angpt1*, *Svep1*, and *Ltbp2* in TMCs (fibroblast-like cells, C1). Gene expression derived from scRNAseq data (normalized log2 fold change, left) alongside tissue sections stained by ISH (right) at each age. All ISH images are oriented the same as first panel (anterior (A) left, posterior (P) right, outer (O) top, and inner (I) bottom). Location of TM between dashed white lines and SC as red ellipse.

Fig. 6: Cellular subtypes and associated gene expression within the developing trabecular meshwork cell population. (A) UMAP plot of seven TMC-like subtypes (TMC0-TMC6) derived from FBL0 at each age. (B) Dot plot of key marker gene expression distinguishing TMC-like subtypes.

Fig. 7: Dot plot visualization of the relative expression of 395 genes selectively expressed in SC- and TM-related cell clusters. Gene names are listed along the y-axis and cell type cluster names are shown along the x-axis; six SC-related clusters (SEC0-SEC5) and seven TM-related clusters (TMC0-TMC6). Average gene expression is relative to other SC and TM clusters.

Fig. 8: Dot plot visualization of the relative expression of 44 Mendelian congenital glaucoma-associated genes between SEC and TMC subtypes.

REFERENCES

1. M. T. García-Antón *et al.*, Goniodysgenesis variability and activity of CYP1B1 genotypes in primary congenital glaucoma. *PLoS One* **12**, e0176386 (2017).
2. T. Souma *et al.*, Angiopoietin receptor TEK mutations underlie primary congenital glaucoma with variable expressivity. *J Clin Invest* **126**, 2575-2587 (2016).
3. B. R. Thomson *et al.*, Angiopoietin-1 is required for Schlemm's canal development in mice and humans. *J Clin Invest* **127**, 4421-4436 (2017).
4. M. H. Kuehn *et al.*, A Mutation in LTBP2 Causes Congenital Glaucoma in Domestic Cats (Felis catus). *PLoS One* **11**, e0154412 (2016).
5. T. van Zyl *et al.*, Cell atlas of aqueous humor outflow pathways in eyes of humans and four model species provides insight into glaucoma pathogenesis. *Proc Natl Acad Sci U S A* **117**, 10339-10349 (2020).
6. T. van Zyl *et al.*, Cell atlas of the human ocular anterior segment: Tissue-specific and shared cell types. *Proc Natl Acad Sci U S A* **119**, e2200914119 (2022).
7. G. Patel *et al.*, Molecular taxonomy of human ocular outflow tissues defined by single-cell transcriptomics. *Proc Natl Acad Sci U S A* **117**, 12856-12867 (2020).
8. B. R. Thomson *et al.*, Cellular crosstalk regulates the aqueous humor outflow pathway and provides new targets for glaucoma therapies. *Nat Commun* **12**, 6072 (2021).
9. R. Balasubramanian *et al.*, Transcriptomic profiling of Schlemm's canal cells reveals a lymphatic-biased identity and three major cell states. *Elife* **13** (2024).
10. W. D. Stamer, A. F. Clark, The many faces of the trabecular meshwork cell. *Exp Eye Res* **158**, 112-123 (2017).
11. R. Fuchshofer, U. Welge-Lüssen, E. Lütjen-Drecoll, M. Birke, Biochemical and morphological analysis of basement membrane component expression in corneoscleral and cribriform human trabecular meshwork cells. *Invest Ophthalmol Vis Sci* **47**, 794-801 (2006).
12. K. Kizhatil, M. Ryan, J. K. Marchant, S. Henrich, S. W. John, Schlemm's canal is a unique vessel with a combination of blood vascular and lymphatic phenotypes that forms by a novel developmental process. *PLoS Biol* **12**, e1001912 (2014).
13. D. Y. Park *et al.*, Lymphatic regulator PROX1 determines Schlemm's canal integrity and identity. *J Clin Invest* **124**, 3960-3974 (2014).
14. S. T. Braakman, J. E. Moore, Jr., C. R. Ethier, D. R. Overby, Transport across Schlemm's canal endothelium and the blood-aqueous barrier. *Exp Eye Res* **146**, 17-21 (2016).
15. C. Remé, U. Urner, B. Aeberhard, The development of the chamber angle in the rat eye. Morphological characteristics of developmental stages. *Graefes Arch Clin Exp Ophthalmol* **220**, 139-153 (1983).
16. A. Aspelund *et al.*, The Schlemm's canal is a VEGF-C/VEGFR-3-responsive lymphatic-like vessel. *J Clin Invest* **124**, 3975-3986 (2014).

17. A. J. Lang *et al.*, Structural organization of the human TOP2A and TOP2B genes. *Gene* **221**, 255-266 (1998).
18. J. Gerdes *et al.*, Cell cycle analysis of a cell proliferation-associated human nuclear antigen defined by the monoclonal antibody Ki-67. *J Immunol* **133**, 1710-1715 (1984).
19. S. Chakarov *et al.*, Two distinct interstitial macrophage populations coexist across tissues in specific subtissular niches. *Science* **363** (2019).
20. C. Köhler, Allograft inflammatory factor-1/Ionized calcium-binding adapter molecule 1 is specifically expressed by most subpopulations of macrophages and spermatids in testis. *Cell Tissue Res* **330**, 291-302 (2007).
21. M. Hsieh *et al.*, Carbonic Anhydrase VIII (CAVIII) Gene Mediated Colorectal Cancer Growth and Angiogenesis through Mediated miRNA 16-5p. *Biomedicines* **10** (2022).
22. H. Yukiura, K. Kano, R. Kise, A. Inoue, J. Aoki, LPP3 localizes LPA6 signalling to non-contact sites in endothelial cells. *J Cell Sci* **128**, 3871-3877 (2015).
23. A. Icking *et al.*, NOSTRIN functions as a homotrimeric adaptor protein facilitating internalization of eNOS. *J Cell Sci* **118**, 5059-5069 (2005).
24. C. Norrmén *et al.*, FOXC2 controls formation and maturation of lymphatic collecting vessels through cooperation with NFATc1. *J Cell Biol* **185**, 439-457 (2009).
25. D. Valdembri, D. Regano, F. Maione, E. Giraudo, G. Serini, Class 3 semaphorins in cardiovascular development. *Cell Adh Migr* **10**, 641-651 (2016).
26. H. Aghajanian *et al.*, Semaphorin 3d and semaphorin 3e direct endothelial motility through distinct molecular signaling pathways. *J Biol Chem* **289**, 17971-17979 (2014).
27. D. J. Lee *et al.*, MAST4 regulates stem cell maintenance with DLX3 for epithelial development and amelogenesis. *Exp Mol Med* **56**, 1606-1619 (2024).
28. J. Matsui, T. Wakabayashi, M. Asada, K. Yoshimatsu, M. Okada, Stem cell factor/c-kit signaling promotes the survival, migration, and capillary tube formation of human umbilical vein endothelial cells. *J Biol Chem* **279**, 18600-18607 (2004).
29. A. E. Koch, M. M. Halloran, C. J. Haskell, M. R. Shah, P. J. Polverini, Angiogenesis mediated by soluble forms of E-selectin and vascular cell adhesion molecule-1. *Nature* **376**, 517-519 (1995).
30. M. D. Buschman *et al.*, The novel adaptor protein Tks4 (SH3PXD2B) is required for functional podosome formation. *Mol Biol Cell* **20**, 1302-1311 (2009).
31. D. Hubmacher *et al.*, Unusual life cycle and impact on microfibril assembly of ADAMTS17, a secreted metalloprotease mutated in genetic eye disease. *Sci Rep* **7**, 41871 (2017).
32. S. M. Craige *et al.*, NADPH oxidase 4 promotes endothelial angiogenesis through endothelial nitric oxide synthase activation. *Circulation* **124**, 731-740 (2011).
33. K. Watanabe *et al.*, Vasohibin as an endothelium-derived negative feedback regulator of angiogenesis. *J Clin Invest* **114**, 898-907 (2004).
34. N. Wick *et al.*, Transcriptomal comparison of human dermal lymphatic endothelial cells ex vivo and in vitro. *Physiol Genomics* **28**, 179-192 (2007).
35. S. Rousseau, F. Houle, J. Landry, J. Huot, p38 MAP kinase activation by vascular endothelial growth factor mediates actin reorganization and cell migration in human endothelial cells. *Oncogene* **15**, 2169-2177 (1997).
36. Q. Zhu, Y. H. Kim, D. Wang, S. P. Oh, K. Luo, SnoN facilitates ALK1-Smad1/5 signaling during embryonic angiogenesis. *J Cell Biol* **202**, 937-950 (2013).
37. A. Mannan, S. Dhiamn, N. Garg, T. G. Singh, Pharmacological modulation of Sonic Hedgehog signaling pathways in Angiogenesis: A mechanistic perspective. *Dev Biol* **504**, 58-74 (2023).
38. S. Elbitar *et al.*, Pathogenic variants in THSD4, encoding the ADAMTS-like 6 protein, predispose to inherited thoracic aortic aneurysm. *Genet Med* **23**, 111-122 (2021).

39. M. D. Gunn *et al.*, A chemokine expressed in lymphoid high endothelial venules promotes the adhesion and chemotaxis of naive T lymphocytes. *Proc Natl Acad Sci U S A* **95**, 258-263 (1998).
40. K. Vaahtomeri, C. Moussion, R. Hauschild, M. Sixt, Shape and Function of Interstitial Chemokine CCL21 Gradients Are Independent of Heparan Sulfates Produced by Lymphatic Endothelium. *Front Immunol* **12**, 630002 (2021).
41. D. Choi *et al.*, Laminar flow downregulates Notch activity to promote lymphatic sprouting. *J Clin Invest* **127**, 1225-1240 (2017).
42. D. Choi *et al.*, Piezo1-Regulated Mechanotransduction Controls Flow-Activated Lymphatic Expansion. *Circ Res* **131**, e2-e21 (2022).
43. Y. Zhao, S. Lin, Essential role of SH3-domain GRB2-like 3 for vascular lumen maintenance in zebrafish. *Arterioscler Thromb Vasc Biol* **33**, 1280-1286 (2013).
44. J. A. Black, S. G. Waxman, Noncanonical roles of voltage-gated sodium channels. *Neuron* **80**, 280-291 (2013).
45. A. Wasik, K. Ratajczak-Wielgomas, A. Badzinski, P. Dziegiel, M. Podhorska-Okolow, The Role of Periostin in Angiogenesis and Lymphangiogenesis in Tumors. *Cancers (Basel)* **14** (2022).
46. F. De Luca, M. Kha, K. Swärd, M. E. Johansson, Identification of ARMH4 and WIPF3 as human podocyte proteins with potential roles in immunomodulation and cytoskeletal dynamics. *PLoS One* **18**, e0280270 (2023).
47. D. Vreeken *et al.*, Downregulation of Endothelial Plexin A4 Under Inflammatory Conditions Impairs Vascular Integrity. *Front Cardiovasc Med* **8**, 633609 (2021).
48. T. Morishita *et al.*, Vasculoprotective roles of neuronal nitric oxide synthase. *Faseb j* **16**, 1994-1996 (2002).
49. V. Kuek *et al.*, NPNT is Expressed by Osteoblasts and Mediates Angiogenesis via the Activation of Extracellular Signal-regulated Kinase. *Sci Rep* **6**, 36210 (2016).
50. B. Simonson *et al.*, Single-nucleus RNA sequencing in ischemic cardiomyopathy reveals common transcriptional profile underlying end-stage heart failure. *Cell Rep* **42**, 112086 (2023).
51. E. Arystarkhova, Beneficial Renal and Pancreatic Phenotypes in a Mouse Deficient in FXYD2 Regulatory Subunit of Na,K-ATPase. *Front Physiol* **7**, 88 (2016).
52. A. L. Williams, B. L. Bohnsack, The Ocular Neural Crest: Specification, Migration, and Then What? *Front Cell Dev Biol* **8**, 595896 (2020).
53. A. Cvekl, E. R. Tamm, Anterior eye development and ocular mesenchyme: new insights from mouse models and human diseases. *Bioessays* **26**, 374-386 (2004).
54. H. Y. Gong, V. Trinkaus-Randall, T. F. Freddo, Ultrastructural immunocytochemical localization of elastin in normal human trabecular meshwork. *Curr Eye Res* **8**, 1071-1082 (1989).
55. W. Xue, R. Wallin, E. A. Olmsted-Davis, T. Borrás, Matrix GLA protein function in human trabecular meshwork cells: inhibition of BMP2-induced calcification process. *Invest Ophthalmol Vis Sci* **47**, 997-1007 (2006).
56. U. R. Chowdhury, S. Y. Jea, D. J. Oh, D. J. Rhee, M. P. Fautsch, Expression profile of the matricellular protein osteopontin in primary open-angle glaucoma and the normal human eye. *Invest Ophthalmol Vis Sci* **52**, 6443-6451 (2011).
57. T. L. Young *et al.*, SVEP1 as a Genetic Modifier of TEK-Related Primary Congenital Glaucoma. *Invest Ophthalmol Vis Sci* **61**, 6 (2020).
58. M. Narooie-Nejad *et al.*, Loss of function mutations in the gene encoding latent transforming growth factor beta binding protein 2, LTBP2, cause primary congenital glaucoma. *Hum Mol Genet* **18**, 3969-3977 (2009).
59. E. Lütjen-Drecoll, Functional morphology of the trabecular meshwork in primate eyes. *Prog Retin Eye Res* **18**, 91-119 (1999).

60. M. A. Shuman, J. R. Polansky, C. Merkel, J. A. Alvarado, Tissue plasminogen activator in cultured human trabecular meshwork cells. Predominance of enzyme over plasminogen activator inhibitor. *Invest Ophthalmol Vis Sci* **29**, 401-405 (1988).
61. M. A. De La Paz, D. L. Epstein, Effect of age on superoxide dismutase activity of human trabecular meshwork. *Invest Ophthalmol Vis Sci* **37**, 1849-1853 (1996).
62. P. B. Liton *et al.*, Induction of IL-6 expression by mechanical stress in the trabecular meshwork. *Biochem Biophys Res Commun* **337**, 1229-1236 (2005).
63. M. Rittig, C. Flügel, P. Prehm, E. Lütjen-Drecoll, Hyaluronan synthase immunoreactivity in the anterior segment of the primate eye. *Graefes Arch Clin Exp Ophthalmol* **231**, 313-317 (1993).
64. T. Usui *et al.*, Hyaluronan synthase in trabecular meshwork cells. *Br J Ophthalmol* **87**, 357-360 (2003).
65. K. E. Keller *et al.*, The effects of tenascin C knockdown on trabecular meshwork outflow resistance. *Invest Ophthalmol Vis Sci* **54**, 5613-5623 (2013).
66. C. Flügel-Koch, A. Ohlmann, R. Fuchshofer, U. Welge-Lüssen, E. R. Tamm, Thrombospondin-1 in the trabecular meshwork: localization in normal and glaucomatous eyes, and induction by TGF-beta1 and dexamethasone in vitro. *Exp Eye Res* **79**, 649-663 (2004).
67. A. Siegner, C. A. May, U. W. Welge-Lüssen, H. Bloemendal, E. Lütjen-Drecoll, alpha B-crystallin in the primate ciliary muscle and trabecular meshwork. *Eur J Cell Biol* **71**, 165-169 (1996).
68. J. G. Walsh *et al.*, Executioner caspase-3 and caspase-7 are functionally distinct proteases. *Proc Natl Acad Sci U S A* **105**, 12815-12819 (2008).
69. K. Matsumoto *et al.*, Distinct interaction of versican/PG-M with hyaluronan and link protein. *J Biol Chem* **278**, 41205-41212 (2003).
70. K. E. Keller, J. M. Bradley, J. A. Vranka, T. S. Acott, Segmental versican expression in the trabecular meshwork and involvement in outflow facility. *Invest Ophthalmol Vis Sci* **52**, 5049-5057 (2011).
71. D. R. McCulloch *et al.*, ADAMTS metalloproteases generate active versican fragments that regulate interdigital web regression. *Dev Cell* **17**, 687-698 (2009).
72. H. S. Dua *et al.*, The collagen matrix of the human trabecular meshwork is an extension of the novel pre-Descemet's layer (Dua's layer). *Br J Ophthalmol* **98**, 691-697 (2014).
73. J. Fang *et al.*, Piezo2 downregulation via the Cre-lox system affects aqueous humor dynamics in mice. *Mol Vis* **27**, 354-364 (2021).
74. D. Docheva, E. B. Hunziker, R. Fassler, O. Brandau, Tenomodulin is necessary for tenocyte proliferation and tendon maturation. *Mol Cell Biol* **25**, 699-705 (2005).
75. K. Runager, J. J. Enghild, G. K. Klintworth, Focus on molecules: Transforming growth factor beta induced protein (TGFBIp). *Exp Eye Res* **87**, 298-299 (2008).
76. K. Harada *et al.*, Identification of targets of Prox1 during in vitro vascular differentiation from embryonic stem cells: functional roles of HoxD8 in lymphangiogenesis. *J Cell Sci* **122**, 3923-3930 (2009).
77. A. S. Ma, J. R. Grigg, R. V. Jamieson, Phenotype-genotype correlations and emerging pathways in ocular anterior segment dysgenesis. *Hum Genet* **138**, 899-915 (2019).
78. O. M. Siggs *et al.*, Prevalence of FOXC1 Variants in Individuals With a Suspected Diagnosis of Primary Congenital Glaucoma. *JAMA Ophthalmol* **137**, 348-355 (2019).
79. O. M. Siggs *et al.*, Biallelic CPAMD8 Variants Are a Frequent Cause of Childhood and Juvenile Open-Angle Glaucoma. *Ophthalmology* **127**, 758-766 (2020).
80. Y. C. Tham *et al.*, Global prevalence of glaucoma and projections of glaucoma burden through 2040: a systematic review and meta-analysis. *Ophthalmology* **121**, 2081-2090 (2014).
81. Y. H. Kwon, J. H. Fingert, M. H. Kuehn, W. L. Alward, Primary open-angle glaucoma. *N Engl J Med* **360**, 1113-1124 (2009).

82. P. Gharahkhani *et al.*, Genome-wide meta-analysis identifies 127 open-angle glaucoma loci with consistent effect across ancestries. *Nat Commun* **12**, 1258 (2021).
83. X. Han *et al.*, Large-scale multitrait genome-wide association analyses identify hundreds of glaucoma risk loci. *Nat Genet* **55**, 1116-1125 (2023).
84. S. Banerji *et al.*, LYVE-1, a new homologue of the CD44 glycoprotein, is a lymph-specific receptor for hyaluronan. *J Cell Biol* **144**, 789-801 (1999).
85. Y. Zhao *et al.*, Cyp1b1 mediates periostin regulation of trabecular meshwork development by suppression of oxidative stress. *Mol Cell Biol* **33**, 4225-4240 (2013).
86. O. Yarishkin *et al.*, Piezo1 channels mediate trabecular meshwork mechanotransduction and promote aqueous fluid outflow. *J Physiol* **599**, 571-592 (2021).
87. J. Du, B. R. Thomson, T. Onay, S. E. Quaggin, Endothelial Tyrosine Kinase Tie1 Is Required for Normal Schlemm's Canal Development-Brief Report. *Arterioscler Thromb Vasc Biol* **42**, 348-351 (2022).
88. S. S. Cheong *et al.*, Mutations in CPAMD8 Cause a Unique Form of Autosomal-Recessive Anterior Segment Dysgenesis. *Am J Hum Genet* **99**, 1338-1352 (2016).
89. J. E. Dulle, A. Rübsam, S. J. Garnai, H. S. Pawar, P. E. Fort, BetaB2-crystallin mutations associated with cataract and glaucoma leads to mitochondrial alterations in lens epithelial cells and retinal neurons. *Exp Eye Res* **155**, 85-90 (2017).
90. S. J. Garnai *et al.*, Congenital cataracts: de novo gene conversion event in CRYBB2. *Mol Vis* **20**, 1579-1593 (2014).
91. H. Liu *et al.*, Crystallins Play a Crucial Role in Glaucoma and Promote Neuronal Cell Survival in an In Vitro Model Through Modulating Müller Cell Secretion. *Invest Ophthalmol Vis Sci* **63**, 3 (2022).
92. E. V. Semina, I. Brownell, H. A. Mintz-Hittner, J. C. Murray, M. Jamrich, Mutations in the human forkhead transcription factor FOXE3 associated with anterior segment ocular dysgenesis and cataracts. *Hum Mol Genet* **10**, 231-236 (2001).
93. A. Blixt *et al.*, A forkhead gene, FoxE3, is essential for lens epithelial proliferation and closure of the lens vesicle. *Genes Dev* **14**, 245-254 (2000).
94. E. V. Semina *et al.*, A novel homeobox gene PITX3 is mutated in families with autosomal-dominant cataracts and ASMD. *Nat Genet* **19**, 167-170 (1998).
95. K. S. Nair *et al.*, Alteration of the serine protease PRSS56 causes angle-closure glaucoma in mice and posterior microphthalmia in humans and mice. *Nat Genet* **43**, 579-584 (2011).
96. A. Rad *et al.*, MAB21L1 loss of function causes a syndromic neurodevelopmental disorder with distinctive cerebellar, ocular, craniofacial and genital features (COFG syndrome). *J Med Genet* **56**, 332-339 (2019).
97. B. Deml *et al.*, Mutations in MAB21L2 result in ocular Coloboma, microcornea and cataracts. *PLoS Genet* **11**, e1005002 (2015).
98. A. L. Bruel *et al.*, Autosomal recessive truncating MAB21L1 mutation associated with a syndromic scrotal agenesis. *Clin Genet* **91**, 333-338 (2017).
99. S. E. Seese, B. Deml, S. Muheisen, E. Sorokina, E. V. Semina, Genetic disruption of zebrafish mab21l1 reveals a conserved role in eye development and affected pathways. *Dev Dyn* **250**, 1056-1073 (2021).
100. S. Wawersik, R. L. Maas, Vertebrate eye development as modeled in Drosophila. *Hum Mol Genet* **9**, 917-925 (2000).
101. I. M. Hanson, PAX6 and congenital eye malformations. *Pediatr Res* **54**, 791-796 (2003).
102. D. C. Baulmann *et al.*, Pax6 heterozygous eyes show defects in chamber angle differentiation that are associated with a wide spectrum of other anterior eye segment abnormalities. *Mech Dev* **118**, 3-17 (2002).

103. J. J. Ferre-Fernández *et al.*, Whole-Exome Sequencing of Congenital Glaucoma Patients Reveals Hypermorphic Variants in GPATCH3, a New Gene Involved in Ocular and Craniofacial Development. *Sci Rep* **7**, 46175 (2017).
104. T. Smith, A. Heger, I. Sudbery, UMI-tools: modeling sequencing errors in Unique Molecular Identifiers to improve quantification accuracy. *Genome Res* **27**, 491-499 (2017).
105. Y. Hao *et al.*, Dictionary learning for integrative, multimodal and scalable single-cell analysis. *Nat Biotechnol* **42**, 293-304 (2024).
106. H. C. T. Nguyen, B. Baik, S. Yoon, T. Park, D. Nam, Benchmarking integration of single-cell differential expression. *Nat Commun* **14**, 1570 (2023).
107. S. E. Marsh, M. Salmon, P. Hoffman (2024) scCustomize: Custom Visualizations & Functions for Streamlined Analyses of Single Cell Sequencing. (Zenodo).

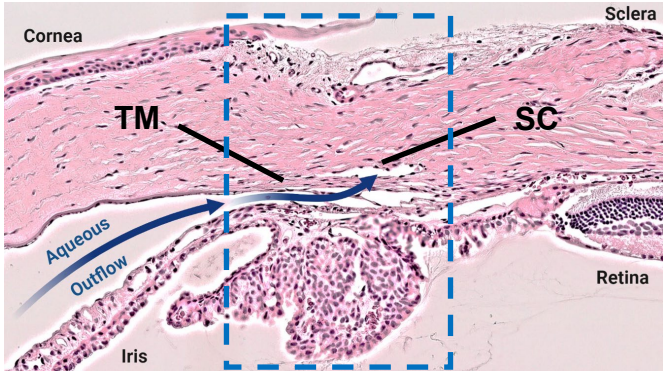

Figure 1

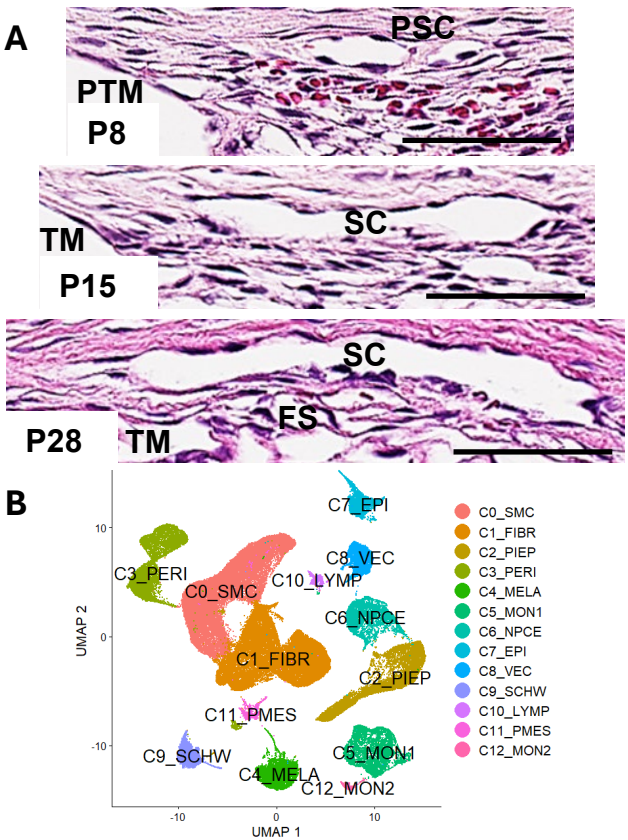
A
PSC
PTM
P8
SC
TM
P15
SC
FS
P28
TM
B
C7_EPI
C8_VEC
C3_PERI
C10_LYMP
C0_SMC
C6_NPCE
C1_FIBR
C2_PIEP
C11_PMES
C9_SCHW
C5_MON1
C4_MELA
C12_MON2
UMAP 2
UMAP 1
10
0
-10
-10
0
10
C0_SMC
C1_FIBR
C2_PIEP
C3_PERI
C4_MELA
C5_MON1
C6_NPCE
C7_EPI
C8_VEC
C9_SCHW
C10_LYMP
C11_PMES
C12_MON2

Figure 2

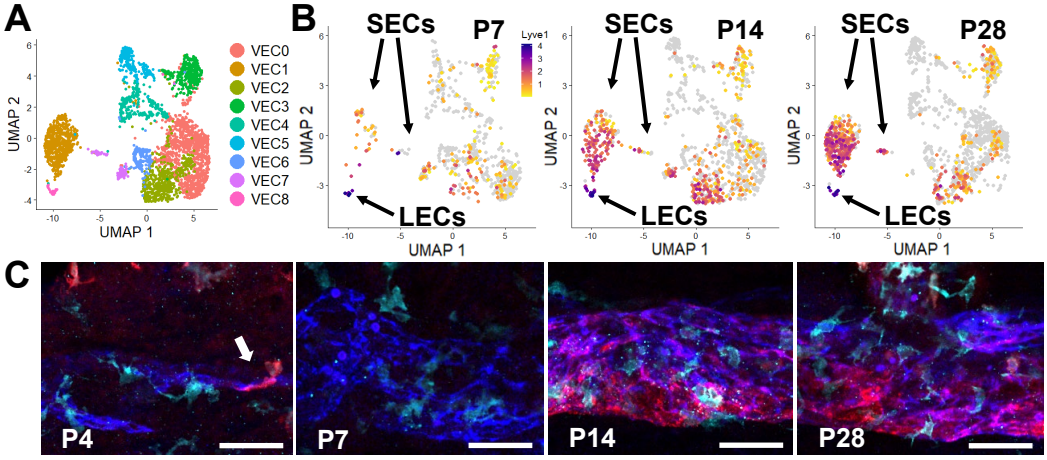
A
UMAP 2
UMAP 1
VEC0
VEC1
VEC2
VEC3
VEC4
VEC5
VEC6
VEC7
VEC8
B
SECs
P7
LECs
Lyve1
SECs
P14
LECs
SECs
P28
LECs
UMAP 2
UMAP 1
C
P4
P7
P14
P28

Figure 3

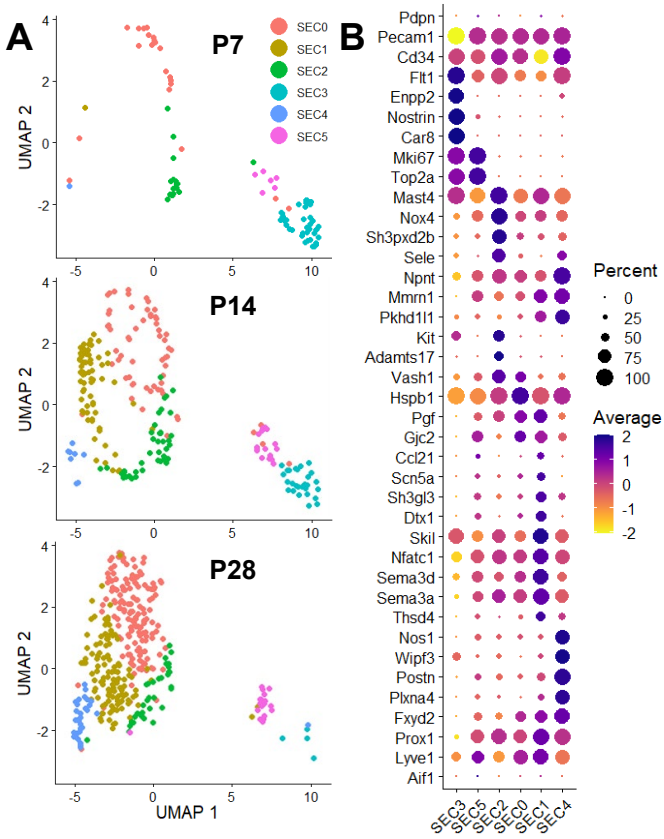
A
P7
P14
P28
SEC0
SEC1
SEC2
SEC3
SEC4
SEC5
UMAP 2
UMAP 1
B
Pdpn
Pecam1
Cd34
Flt1
Enpp2
Nostrin
Car8
Mki67
Top2a
Mast4
Nox4
Sh3pxd2b
Sele
Npnt
Mmrn1
Pkhd1l1
Kit
Adamts17
Vash1
Hspb1
Pgf
Gjc2
Ccl21
Scn5a
Sh3gl3
Dtx1
Skil
Nfatc1
Sema3d
Sema3a
Thsd4
Nos1
Wipf3
Postn
Plxna4
Fxyd2
Prox1
Lyve1
Aif1
SEC3
SEC5
SEC2
SEC0
SEC1
SEC4
Percent
0
25
50
75
100
Average
2
1
0
-1
-2

Figure 4

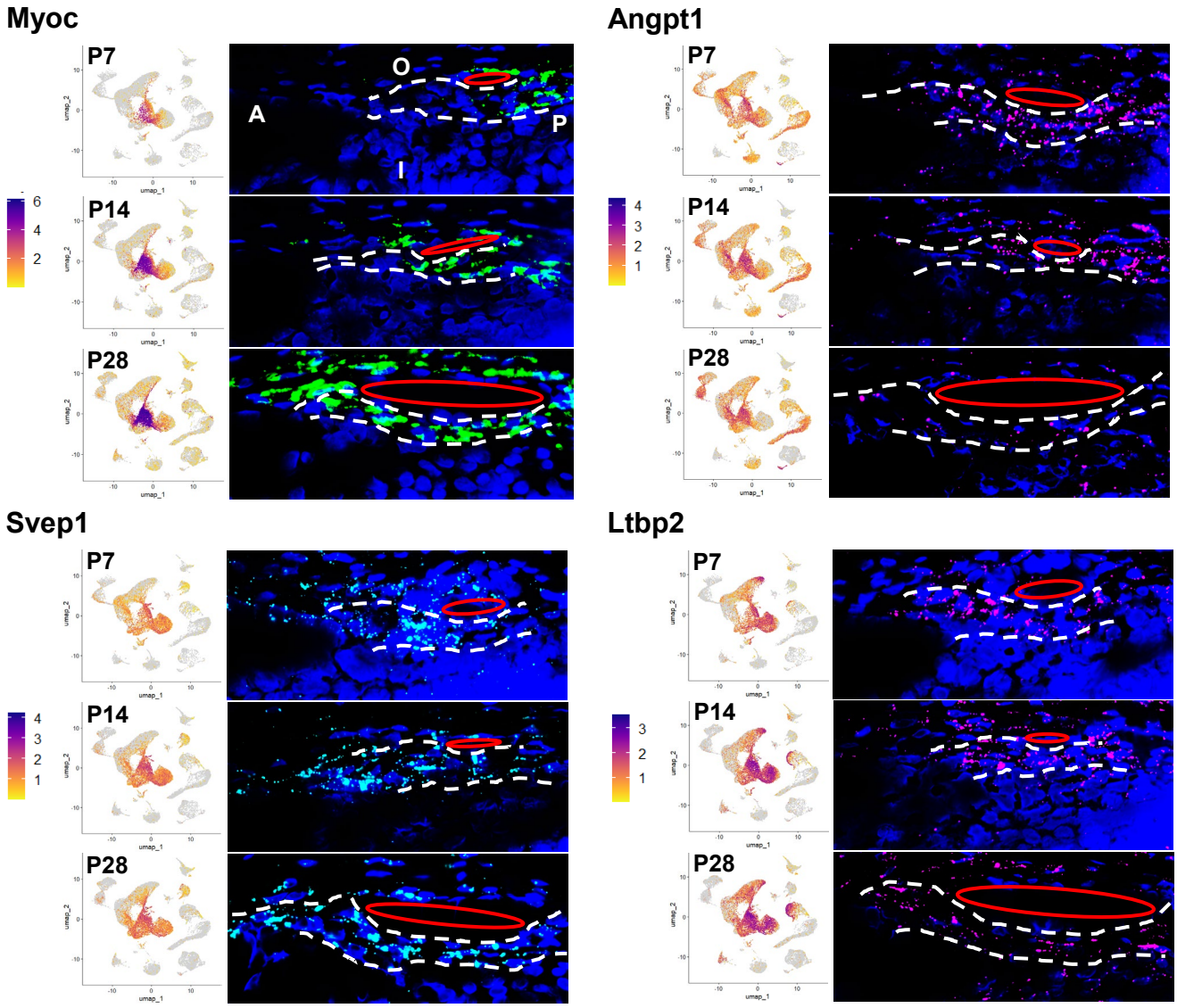
Myoc
P7
P14
P28
O
A
P
I
6
4
2
Angpt1
P7
P14
P28
4
3
2
1
Svep1
P7
P14
P28
4
3
2
1
Ltbp2
P7
P14
P28
3
2
1

Figure 5

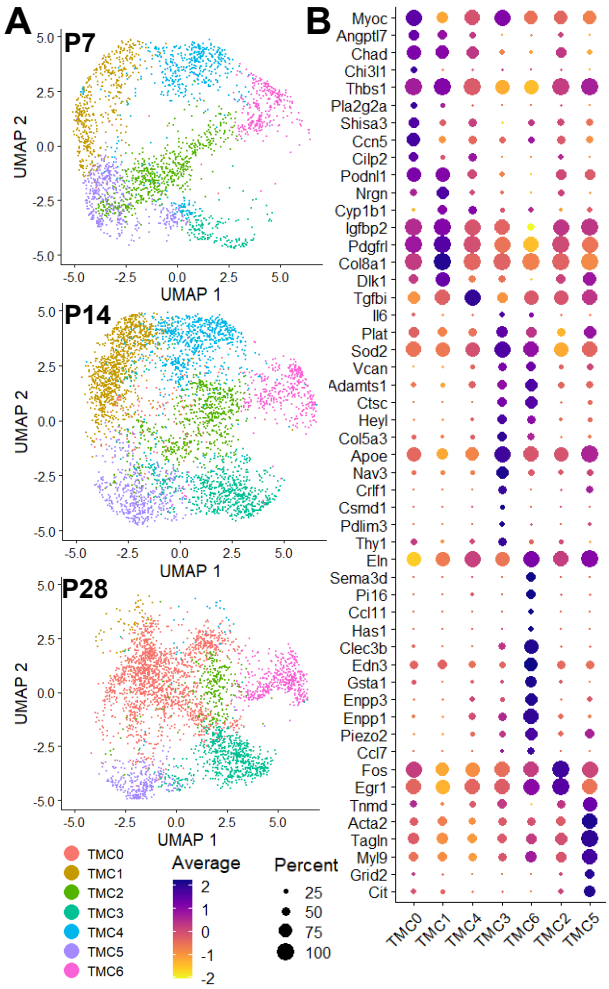
A
P7
P14
P28
UMAP 1
UMAP 2
5.0
2.5
0.0
-2.5
-5.0
TMC0
TMC1
TMC2
TMC3
TMC4
TMC5
TMC6
Average
2
1
0
-1
-2
Percent
25
50
75
100
B
Myoc
Angptl7
Chad
Chi3l1
Thbs1
Pla2g2a
Shisa3
Ccn5
Cilp2
Podnl1
Nrgn
Cyp1b1
Igfbp2
Pdgfrl
Col8a1
Dlk1
Tgfbi
Il6
Plat
Sod2
Vcan
Adamts1
Ctsc
Heyl
Col5a3
Apoe
Nav3
Crlf1
Csmd1
Pdlim3
Thy1
Eln
Sema3d
Pi16
Ccl11
Has1
Clec3b
Edn3
Gsta1
Enpp3
Enpp1
Piezo2
Ccl7
Fos
Egr1
Tnmd
Acta2
Tagln
Myl9
Grid2
Cit
TMC0
TMC1
TMC4
TMC3
TMC6
TMC2
TMC5

Figure 6

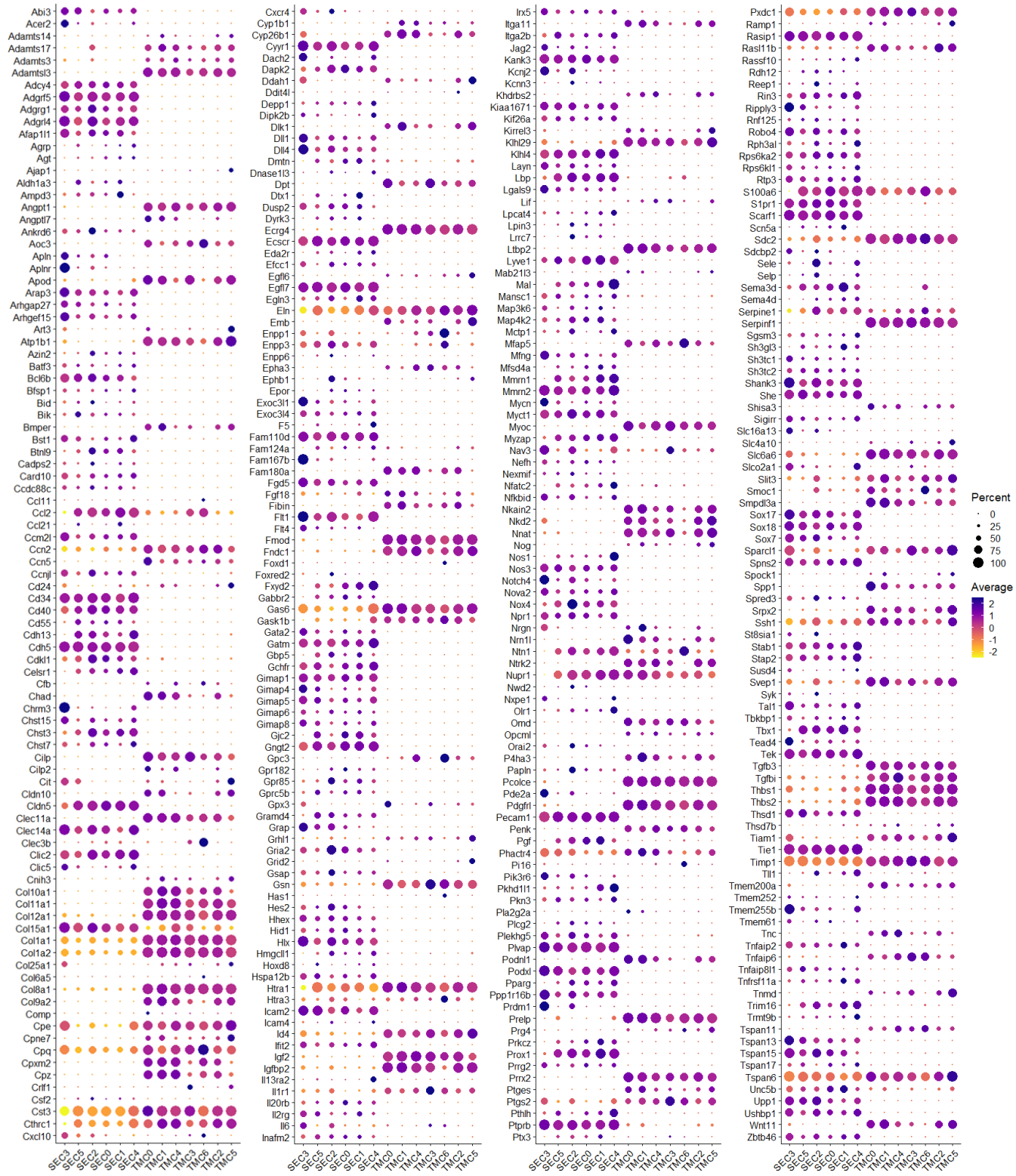
Abi3
Acer2
Adamts14
Adamts17
Adamts3
Adamtsl3
Adcy4
Adgrf5
Adgrg1
Adgrl4
Afap1l1
Agrp
Agt
Ajap1
Aldh1a3
Ampd3
Angpt1
Angptl7
Ankrd6
Aoc3
Apln
Aplnr
Apod
Arap3
Arhgap27
Arhgef15
Art3
Atp1b1
Azin2
Batf3
Bcl6b
Bfsp1
Bid
Bik
Bmper
Bst1
Btnl9
Cadps2
Card10
Ccdc88c
Ccl11
Ccl2
Ccl21
Ccm2l
Ccn2
Ccn5
Ccnjl
Cd24
Cd34
Cd40
Cd55
Cdh13
Cdh5
Cdkl1
Celsr1
Cfb
Chad
Chrm3
Chst15
Chst3
Chst7
Cilp
Cilp2
Cit
Cldn10
Cldn5
Clec11a
Clec14a
Clec3b
Clic2
Clic5
Cnih3
Col10a1
Col11a1
Col12a1
Col15a1
Col1a1
Col1a2
Col25a1
Col6a5
Col8a1
Col9a2
Comp
Cpe
Cpne7
Cpq
Cpxm2
Cpz
Crlf1
Csf2
Cst3
Cthrc1
Cxcl10
Cxcr4
Cyp1b1
Cyp26b1
Cyyr1
Dach2
Dapk2
Ddah1
Ddit4l
Depp1
Dipk2b
Dlk1
Dll1
Dll4
Dmtn
Dnase1l3
Dpt
Dtx1
Dusp2
Dyrk3
Ecrg4
Ecscr
Eda2r
Efcc1
Egfl6
Egfl7
Egln3
Eln
Emb
Enpp1
Enpp3
Enpp6
Epha3
Ephb1
Epor
Exoc3l1
Exoc3l4
F5
Fam110d
Fam124a
Fam167b
Fam180a
Fgd5
Fgf18
Fibin
Flt1
Flt4
Fmod
Fndc1
Foxd1
Foxred2
Fxyd2
Gabbr2
Gas6
Gask1b
Gata2
Gatm
Gbp5
Gchfr
Gimap1
Gimap4
Gimap5
Gimap6
Gimap8
Gjc2
Gngt2
Gpc3
Gpr182
Gpr85
Gprc5b
Gpx3
Gramd4
Grap
Grhl1
Gria2
Grid2
Gsap
Gsn
Has1
Hes2
Hhex
Hid1
Hlx
Hmgcll1
Hoxd8
Hspa12b
Htra1
Htra3
Icam2
Icam4
Id4
Ifit2
Igf2
Igfbp2
Il13ra2
Il1r1
Il20rb
Il2rg
Il6
Inafm2
Irx5
Itga11
Itga2b
Jag2
Kank3
Kcnj2
Kcnn3
Khdrbs2
Kiaa1671
Kif26a
Kirrel3
Klhl29
Klhl4
Layn
Lbp
Lgals9
Lif
Lpcat4
Lpin3
Lrrc7
Ltbp2
Lyve1
Mab21l3
Mal
Mansc1
Map3k6
Map4k2
Mctp1
Mfap5
Mfng
Mfsd4a
Mmrn1
Mmrn2
Mycn
Myct1
Myoc
Myzap
Nav3
Nefh
Nexmif
Nfatc2
Nfkbid
Nkain2
Nkd2
Nnat
Nog
Nos1
Nos3
Notch4
Nova2
Nox4
Npr1
Nrgn
Nrn1l
Ntn1
Ntrk2
Nupr1
Nwd2
Nxpe1
Olr1
Omd
Opcml
Orai2
P4ha3
Papln
Pcolce
Pde2a
Pdgfrl
Pecam1
Penk
Pgf
Phactr4
Pi16
Pik3r6
Pkhd1l1
Pkn3
Pla2g2a
Plcg2
Plekhg5
Plvap
Podnl1
Podxl
Pparg
Ppp1r16b
Prdm1
Prelp
Prg4
Prkcz
Prox1
Prrg2
Prrx2
Ptges
Ptgs2
Pthlh
Ptprb
Ptx3
Pxdc1
Ramp1
Rasip1
Rasl11b
Rassf10
Rdh12
Reep1
Rin3
Ripply3
Rnf125
Robo4
Rph3al
Rps6ka2
Rps6kl1
Rtp3
S100a6
S1pr1
Scarf1
Scn5a
Sdc2
Sdcbp2
Sele
Selp
Sema3d
Sema4d
Serpine1
Serpinf1
Sgsm3
Sh3gl3
Sh3tc1
Sh3tc2
Shank3
She
Shisa3
Sigirr
Slc16a13
Slc4a10
Slc6a6
Slco2a1
Slit3
Smoc1
Smpdl3a
Sox17
Sox18
Sox7
Sparcl1
Spns2
Spock1
Spp1
Spred3
Srpx2
Ssh1
St8sia1
Stab1
Stap2
Susd4
Svep1
Syk
Tal1
Tbkbp1
Tbx1
Tead4
Tek
Tgfb3
Tgfbi
Thbs1
Thbs2
Thsd1
Thsd7b
Tiam1
Tie1
Timp1
Tll1
Tmem200a
Tmem252
Tmem255b
Tmem61
Tnc
Tnfaip2
Tnfaip6
Tnfaip8l1
Tnfrsf11a
Tnmd
Trim16
Trmt9b
Tspan11
Tspan13
Tspan15
Tspan17
Tspan6
Unc5b
Upp1
Ushbp1
Wnt11
Zbtb46
SEC3
SEC5
SEC2
SEC0
SEC1
SEC4
TMC0
TMC1
TMC4
TMC3
TMC6
TMC2
TMC5
Percent
0
25
50
75
100
Average
2
1
0
-1
-2

Figure 7

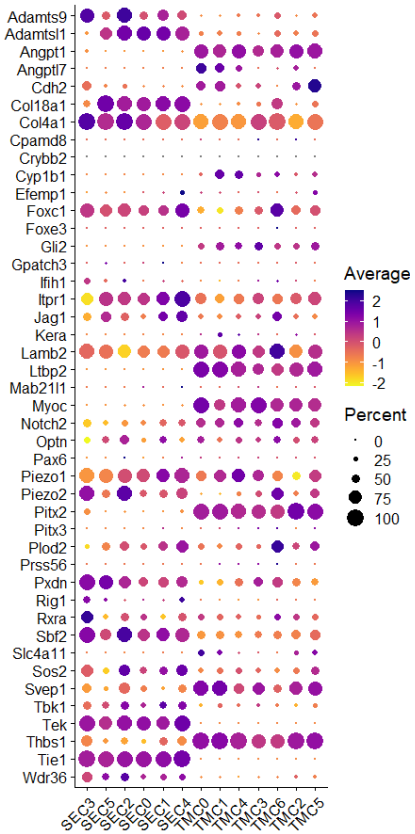
Adamts9
Adamtsl1
Angpt1
Angptl7
Cdh2
Col18a1
Col4a1
Cpamd8
Crybb2
Cyp1b1
Efemp1
Foxc1
Foxe3
Gli2
Gpatch3
Ifih1
Itpr1
Jag1
Kera
Lamb2
Ltbp2
Mab21l1
Myoc
Notch2
Optn
Pax6
Piezo1
Piezo2
Pitx2
Pitx3
Plod2
Prss56
Pxdn
Rig1
Rxra
Sbf2
Slc4a11
Sos2
Svep1
Tbk1
Tek
Thbs1
Tie1
Wdr36
SEC3
SEC5
SEC2
SEC0
SEC1
SEC4
TMC0
TMC1
TMC4
TMC3
TMC6
TMC2
TMC5
Average
2
1
0
-1
-2
Percent
0
25
50
75
100

Figure 8